Title: Nanocrystalline copper films are never flat

Authors: Xiaopu Zhang,[1] Jian Han,[2] John J. Plombon,[3] Adrian P. Sutton,[4] David J. Srolovitz,[2,5] John J. Boland[1*]

Affiliations:

[1]Centre for Research on Adaptive Nanostructures and Nanodevices (CRANN) and School of Chemistry, Trinity College Dublin, Dublin 2, Ireland

[2]Department of Materials Science and Engineering, University of Pennsylvania, Philadelphia, PA 19104 USA

[3]Components Research, Intel Corporation, Hillsboro, Oregon 97124, USA

[4]Department of Physics, Imperial College London, Exhibition Road, London SW7 2AZ, UK

[5]Department of Mechanical Engineering and Applied Mechanics, University of Pennsylvania, Philadelphia, PA 19104 USA

*Correspondence to: jboland@tcd.ie

Abstract: Scanning tunneling microscopy is used to study low angle grain boundaries at the surface of nearly planar copper nanocrystalline (111) films. The presence of grain boundaries and their emergence at the film surface create valleys composed of dissociated edge dislocations and ridges where partial dislocations have recombined. Geometric analysis and simulations confirm valleys and ridges are created by an out-of-plane grain rotation driven by reduction of grain boundary energy. These results indicate that in general it is impossible to form flat two-dimensional nanoscale films of copper and other metals exhibiting small stacking fault energies and/or large elastic anisotropy.

Main Text:

Nanocrystalline metal materials are widely used as electrical contacts and interconnects in ultra-large-scale integrated circuits (*1*). Technologically important properties of these materials (*2-4*) are strongly influenced by the presence and density of surfaces, grain boundaries (GBs) and dislocations within them; each studied extensively (*5-7*). Using transmission electron microscopy (TEM), GBs with high-symmetry tilt axes have been intensively studied at the atomic scale (*8*), where TEM provides a plan view of atomic columns along the tilt axis of the GB. At the granular length scale, the formation, rotation and coalescence of sub-grains during annealing have also been studied by TEM (*7, 9*). Here, we present the first investigation of nanocrystalline metal films from the multi-grain scale down to the atomic scale using scanning tunneling microscopy (STM). Uniquely, STM can map the local three-dimensional topography of GB intersections at surfaces with picometer precision and is insensitive to the degree of tilt axis misalignment from high symmetry directions that typically hampers TEM analysis of GB structure (*10, 11*). We identify shifts in the GB tilt axis away from that of the original low angle GB (LAGB) in nanocrystalline copper films. We show this phenomenon is accompanied by GB energy minimization and results in the unavoidable introduction of ridges and valleys into the film.

High quality nanocrystalline copper films are prepared by physical vapor deposition on top of a 7 nm tantalum coated silicon wafer at room temperature. The copper films have thicknesses of 20 or 50 nm. The sample is etched with glacial acetic acid and loaded into an ultrahigh vacuum system equipped with a low temperature STM. After gentle sputtering and annealing at ~300℃ the surface is atomically clean with rms roughness 0.5 nm over a micron scale. The grain diameter is on the order of the film thickness. The grain surfaces were all (111) oriented, as confirmed by both atomic resolution STM images and *ex-situ* electron Kikuchi diffraction.

Figure 1(A) shows a perspective view of the topography of the copper nanocrystalline thin film. In addition to expected perfect 0.21 nm high surface steps (red arrow), the surface displays ridges and valleys, highlighted by the green and white arrows respectively where GBs emerge at the surface. For the valley location shown in Fig. 1(A) there is a 2.4° misalignment between the [111] normal of the two adjoining grains; the (111) surfaces of these grains are atomically flat. In Figs. 1-2 the (111) surfaces on either side of the grain boundary meet along a line in the boundary plane, suggesting that this GB has pure tilt character.

The valley GB in Fig. 2(A) comprises a sequence of dislocations. The Burgers circuit outlined in green encloses the entire distorted region associated with one of these dislocations. The closure failure of the Burgers circuit is the distance between two nearest-neighbor atoms in the (111) plane, which is $a/\sqrt{2}$, where a is the lattice constant. This is the magnitude of the Burgers vector of a perfect lattice dislocation in Cu. Using the measured step heights associated with these dislocations we may deduce their possible Burgers vectors. Cu has a relatively small stacking fault (SF) energy of ~41 mJ/m^2 (*12*); therefore, lattice dislocations normally dissociate into $a/6\langle 112\rangle$ Shockley partials separated by SFs. The sum of the step heights of each pair of Shockley partials, taking into account their senses, is equal to the step height of the lattice dislocation from which they were formed. A Burgers vector of $a/2[1\bar{1}0]$ dissociates into $a/6\,[2\bar{1}1] + a/6\,[1\bar{2}\bar{1}]$ Shockley partials. The first Shockley partial produces a step up on the (111) surface of height $a/6\,[2\bar{1}1]\cdot[111]/\sqrt{3} = a/3\sqrt{3} = 70$ pm, which is one third of the (111) interplanar spacing. This is consistent with the measured step-profile in Fig 2(B) and earlier measurements *(11)*. The second Shockley partial produces an equal and opposite step down (see inset of Fig. 2(B) where two partials are explicitly shown). The two partials have finite core widths; hence the ± 70 pm step profile are spread out rather than abrupt.

We find GBs at valley and ridge locations have different corrugation amplitudes, see Fig. 1(B) and (C). The corrugation along the valley GB is between 60 pm and 80 pm, consistent with a series of Shockley partial pairs, whereas along the ridge it is smaller ~ 30 pm (Fig. 1D). Figure 2(C) shows a GB with atomic resolution at a ridge. Burgers circuits reveal undissociated dislocations and the location of each edge dislocation core is precisely determined. This is different from the dissociated lattice dislocations in the GBs observed in valleys and is consistent with the breakdown of inversion symmetry of copper (111) films.

To explain how grain tilting gives rise to the ridge and valley features seen in STM, we begin by considering the in-plane misorientation and assume that the dislocation lines are parallel to the surface normal [111]. The GB in Fig. 2(A) displays a periodic sequence of edge dislocations. The solid lines and dotted lines run along the $[\bar{1}\bar{1}2]$ and $[1\bar{1}0]$ directions in the adjoining grains, respectively. The repeat vectors $\vec{\boldsymbol{p}}$ in the boundary plane of the two adjoining crystals are $(4+4+3)a/4\,[\bar{1}\bar{1}2] \pm 3a/4\,[1\bar{1}0] = a/2\,[\bar{4}\,\bar{7}\,11]$ and $a/2\,[\bar{7}\,\bar{4}\,11]$, each of length $p = a\sqrt{186}/2$ (see Fig. 2A). The Burgers vector content $B = 3a/\sqrt{2}$ in each period $\vec{\boldsymbol{p}}$ is related to the

boundary misorientation θ by Frank's formula, $\sin(\theta/2) = B/(2p)$. The estimated value $\theta = 17.9°$ is close to the measured angle $16.2°$ in Fig. 2(A). Therefore, the GB in Fig. 2(A) is a symmetric tilt GB whose boundary lies along the mean of the $(1\bar{1}0)$ planes of the adjoining grains.

However, it is unlikely the dislocation lines are parallel to the surface normal $[111]$ because the SF ribbon plane between the partials would be $(11\bar{2})$ (on average). The low energy SFs in Cu are on $\{111\}$ planes, not $\{112\}$ planes. If the dislocation lines are parallel to $[112]$, which is $19.47°$ from the $[111]$ surface normal, the SFs can be on low energy $(11\bar{1})$ planes. To minimize the SF energy, it is likely that the direction of the dislocation lines, and hence that of the composite rotation axis of the GB, lies somewhere between $[111]$ and $[112]$, which is confirmed directly by simulation below.

To effect this change, we introduce a second rotation so that the GB rotation comprises a rotation $\boldsymbol{\rho_1} = 1/\sqrt{3}\,[111]\tan(\theta/2)$ followed by a rotation $\boldsymbol{\rho_2} = \hat{\boldsymbol{g}}\,\tan(\varphi/2)$, such that the composite rotation (5)

$$\boldsymbol{\rho} = \boldsymbol{\rho_2} * \boldsymbol{\rho_1} \stackrel{\text{def}}{=} \frac{\boldsymbol{\rho_1} + \boldsymbol{\rho_2} - \boldsymbol{\rho_1} \times \boldsymbol{\rho_2}}{1 - \boldsymbol{\rho_1} \cdot \boldsymbol{\rho_2}} \tag{1}$$

is perpendicular to $[1\bar{1}0]$. It follows then from Eq. (1) that $\hat{\boldsymbol{g}} = \cos(\theta/2)\left(1/\sqrt{6}\right)\,[\bar{1}\bar{1}2] + \sin(\theta/2)\left(1/\sqrt{2}\right)[1\bar{1}0]$ and the Rodrigues vector of the composite rotation is:

$$\boldsymbol{\rho} = \tan(\theta/2)\left(\frac{\tan(\varphi/2)}{\sin(\theta/2)}\frac{1}{\sqrt{6}}[\bar{1}\bar{1}2] + \frac{1}{\sqrt{3}}[111]\right) \tag{2}$$

which insures that each dislocation has no net step height at the surface. The angle ψ between $[111]$ and the composite rotation axis, which is also the inclination angle between $[111]$ and the dislocation lines, follows directly from Eq. (2): $\tan\psi = \tan(\varphi/2)/\sin(\theta/2)$. For small θ, this reduces to $\varphi \approx \theta\,\tan(\psi)$.

More generally, $\hat{\boldsymbol{g}}$ is parallel to the blue vector in the boundary plane normal to $[111]$ as shown in Fig. 3(A). Thus, $\boldsymbol{\rho_2}$ is a rotation about an axis lying in the boundary plane which tilts the (111) surfaces on either side of the GB through the angle φ creating a valley or ridge. During the $\boldsymbol{\rho_2}$ rotation, the GB boundary plane remains along the mean of the $(1\bar{1}0)$ planes and bisects the (111) planes of the adjoining grains (see Fig 3(A)). The rotation $\boldsymbol{\rho_2}$ inclines the direction of the dislocation lines towards $[112]$. In the limit where $\tan\psi = 1/\left(2\sqrt{2}\right)$ (i.e., $\psi = 19.47°$), the dislocation lines are entirely parallel to $[112]$.

The distribution of experimentally measured values of θ and φ are shown in Fig. 3(B). Each open (closed) circle represents a GB at a valley (ridge); there is no obvious difference between the data at ridge and valley locations. The red line in Fig. 3(B) is a plot of $\tan\psi = \tan(\varphi/2)/\sin(\theta/2)$ with $\psi = 19.47°$, which sets the upper limit of the out-of-plane grain rotation φ for a given in-plane rotation θ. The black line with slope 0.25 is a linear fit to the data for valley GBs. This means that on average the dislocation line is inclined $14.04°$ from $[111]$ direction instead of $19.47°$. As discussed in the SI we attribute this 5° difference to the Cu-Ta interface, which limits the tilting of the Cu (111) planes.

We calculate the energies of GBs in free-standing (111) films using molecular statics with periodic boundary conditions and an embedded atom method interatomic potential (Fig. S1 and Table S1) (*13*). Each repeat cell contains two GBs with equal and opposite misorientations. The GB structures are relaxed into their lowest energy states for combinations of prescribed in-plane

and out-of-plane rotation angles, θ and φ, respectively. When a GB creates a valley at the top surface of the film, it produces a ridge at the bottom surface, and *vice versa* (see Fig. 3(A)). The GB energy as a function of the inclination angle ψ is shown in Fig. 3(C). Regardless of the in-plane angle θ, the GB energy is minimized at $\psi = 19.47°$. This confirms the out-of-plane rotation φ arises to reduce the GB energy by aligning the dislocation lines along $[112]$, which enables SFs between the partial dislocations to be entirely on low energy $(11\bar{1})$ planes, yielding larger partial dislocation spacings and lower elastic energy.

Simulations also confirm our film-tilting analysis at the atomic scale. The atomic structures of GBs with an in-plane rotation $\theta = 3.89°$ and three out-of-plane angles φ are shown in Fig. 4 from different viewing directions. When $\varphi = 0$ (Fig. 4A), the SF ribbon is in the $(11\bar{2})$ plane on average and is composed of narrow facets of high energy (001) faults between $(11\bar{1})$ facets. As φ increases, we find an increased inclination angle and wider SF ribbons with fewer jogs along their lengths and wider dislocation terminals at the surface, as shown in Fig. 4B. When $\varphi = 1.37°$ (Fig. 4C), corresponding to $\psi = 19.47°$, there are no jogs along the SF ribbon and the partial dislocation separation is maximized. Figure 4 (B-C) also show that the SF ribbon is wider at the where the GB forms a valley (top surface), than where it forms a ridge (bottom surface). This trend is consistent with our experimental observation (Fig. 2C); although in the experiment the partial dislocation separation appears to reduce further than in the simulations (to near zero).

The occurrence of ridges and valleys at emerging low angle tilt boundaries reported here can be generalized to copper films with different surface orientations. Elimination of jogs and high energy fault planes between dissociated dislocations requires both the dislocation line direction and Burgers vector to be in the same $\{111\}$ plane. Of the low index surface orientations, only $\{112\}$ films are expected to be immune. The principles set forth here can also be extended to other FCC films by considering the energy anisotropy of dislocation lines. Based on the results presented here, ridges and valleys are likely to occur at surfaces of nanoscale films of materials with low SF energy and/or high elastic anisotropy such as Ag, Au and Ni. This is particularly important for evaporated and sputtered nanocrystalline metallic films, which under typical deposition conditions exhibit a fiber columnar texture with a significant percentage of LAGBs (*14*).

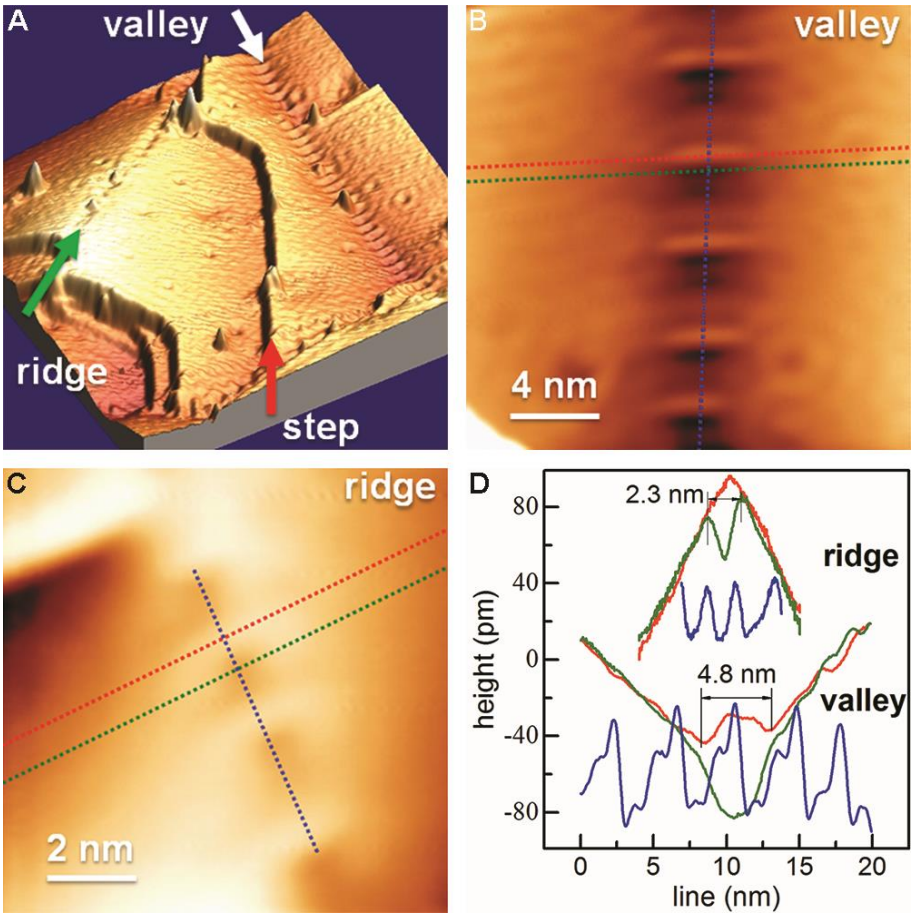

Fig. 1. GBs at ridges and valleys in (111) films of Cu.

(A) Perspective view of the STM topography of nanocrystalline copper film. GBs at ridge and valley location are highlighted by arrows. (B) Close-up view of one GB at valley location. (C) Close-up view of one GB at ridge location. (D) Profile of valley and ridge line cross-sections recorded in (B) and (C), respectively.

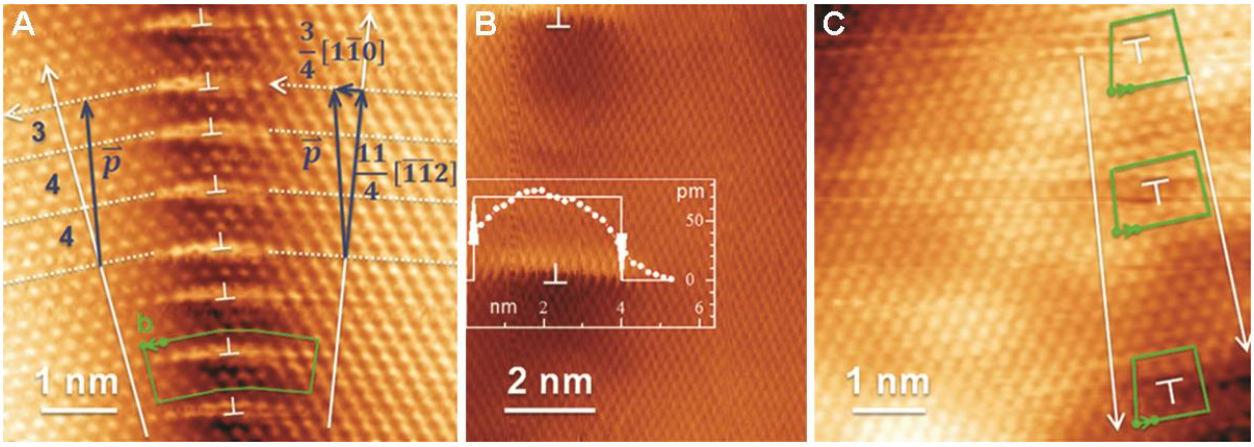

Fig. 2. Atomic structure of emergent LAGBs.

(A) Atomic resolution STM image of a valley GB segment with ~3° out-of-plane angle. The green path shows a Burgers circuit. White dotted lines are along $[1\bar{1}0]$ and solid lines along $[\bar{1}\bar{1}2]$. The repeat sequence 3, 4, 4 is shown along $[\bar{1}\bar{1}2]$. The components of $\vec{\boldsymbol{p}}$ are shown in unit of *a*. The measured boundary misorientation angle θ between the grains is 16.2°. (B) Atomic resolution STM image of a second valley GB area with a smaller out-of-plane angle. The image contains two dissociated edge dislocations across the GB. Inset in (B) is the actual step profile (dotted lines) of the dissociated edge dislocation, including the equal and opposite Shockley partials (arrows). (C) Atomic resolution image of one segment of GB at a ridge location.

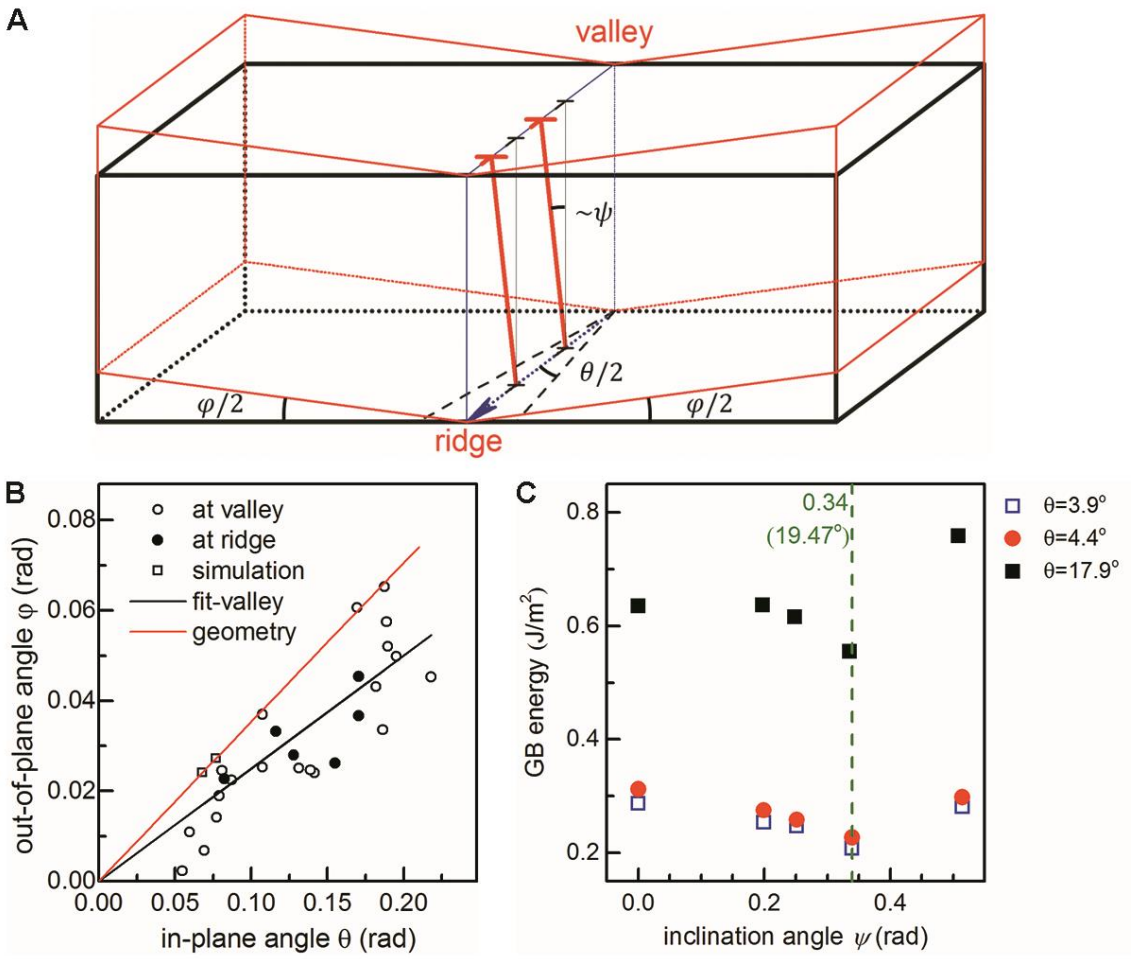

Fig. 3. Relation between in-plane θ and out-of-plane φ rotations and calculated GB energy. (A) Schematic of LAGB induced film tilting at in-plane angle θ and out-of-plane angle φ that shows the inclination angle ψ between the dislocation line and the [111] surface normal. (B) Experimentally measured in-plane θ and out-of-plane φ rotations. (C) Calculated GB energy dependence on the inclination angle ψ for a range of in-plane angles θ. Note each exhibits a minimum at ψ=19.47°.

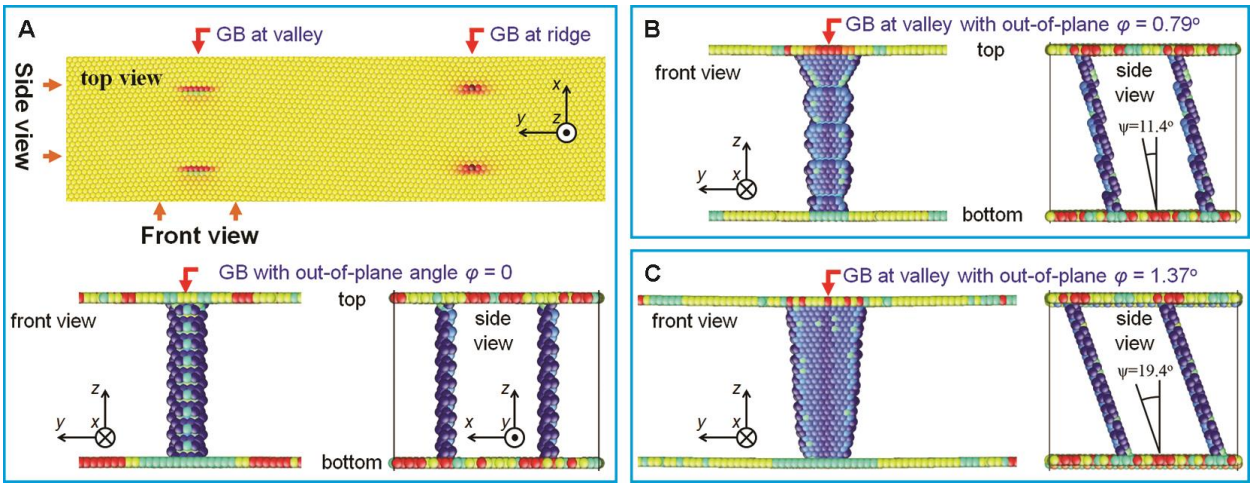

Fig. 4. Molecular statics calculation of LAGBs with $\theta = 3.89°$.

Out-of-plane rotation angle are $\varphi = 0$ (A), $\varphi = 0.79°$ (B) and $\varphi = 1.37°$ (C). Atoms are colored by central symmetry and hence only defect atoms are visible. Front views show that the density reduction of jogs and increasing separation of the partials as ψ approaches $\varphi = 19.4°$. Side views shows the inclination of two SFs of one GB. Top view demonstrates the breakdown of inversion symmetry.

Acknowledgments:

J.J.B. acknowledges the Science Foundation Ireland funded Principal Investigator Award (Grant No. 12/IA/1482) and emanated from research supported in part by a research grant from Science Foundation Ireland (SFI) under Grant Number SFI/12/RC/2278).

Supplementary Materials:

Supplementary Text

Figures S1-S2

Table S1

References (*15, 16*)

References and Notes:

1. International technology roadmap for semiconductors (ITRS), Interconnects Section. *Semiconductor Industry Association*, (2013).
2. K. Lu, L. Lu, S. Suresh, Strengthening Materials by Engineering Coherent Internal Boundaries at the Nanoscale. *Science* **324**, 349-352 (2009).
3. B. Wu, A. Heidelberg, J. J. Boland, Mechanical properties of ultrahigh-strength gold nanowires. *Nat Mater* **4**, 525-529 (2005).
4. J. R. Greer, J. T. M. De Hosson, Plasticity in small-sized metallic systems: Intrinsic versus extrinsic size effect. *Prog Mater Sci* **56**, 654-724 (2011).
5. A. P. Sutton, R. W. Balluffi, *Interfaces in Crystalline Materials*. (OUP Oxford, 2006).
6. J. P. Hirth, J. Lothe, *Theory of Dislocations*. (Graw-Hill, 1982).
7. A. Rollett, F. Humphreys, G. S. Rohrer, M. Hatherly, *Recrystallization and related annealing phenomena*. (Elsevier, 2004).
8. G. Duscher, M. F. Chisholm, U. Alber, M. Ruhle, Bismuth-induced embrittlement of copper grain boundaries. *Nat Mater* **3**, 621-626 (2004).
9. J. C. Li, Possibility of subgrain rotation during recrystallization. *Journal of Applied Physics* **33**, 2958-2965 (1962).
10. J. Christiansen *et al.*, Atomic-scale structure of dislocations revealed by scanning tunneling microscopy and molecular dynamics. *Phys Rev Lett* **88**, 206106 (2002).
11. A. Samsavar *et al.*, High-Resolution Imaging of a Dislocation on Cu(111). *Phys Rev Lett* **65**, 1607-1610 (1990).
12. D. J. Cockayne, M. L. Jenkins, I. L. F. Ray, Measurement of Stacking-Fault Energies of Pure Face-Centred Cubic Metals. *Philos Mag* **24**, 1383-1392 (1971).
13. Y. Mishin, M. J. Mehl, D. A. Papaconstantopoulos, A. F. Voter, J. D. Kress, Structural stability and lattice defects in copper: Ab initio, tight-binding, and embedded-atom calculations. *Phys Rev B* **63**, 224106 (2001).
14. J. M. E. Harper, K. P. Rodbell, Microstructure control in semiconductor metallization. *J Vac Sci Technol B* **15**, 763-779 (1997).
15. S. Plimpton, Fast Parallel Algorithms for Short-Range Molecular-Dynamics. *J Comput Phys* **117**, 1-19 (1995).
16. A. Hashibon, A. Y. Lozovoi, Y. Mishin, C. Elsasser, P. Gumbsch, Interatomic potential for the Cu-Ta system and its application to surface wetting and dewetting. *Phys Rev B* **77**, (2008).